

# 高强铝合金 7075 激光粉末床熔融凝固裂纹的消除与质量控制

吕新蕊<sup>1,2</sup>, 刘婷婷<sup>1,2\*</sup>, 廖文和<sup>1,2</sup>, 韦辉亮<sup>1,2</sup>, 杨涛<sup>1,2</sup>, 蒋立异<sup>1,2</sup>

<sup>1</sup>南京理工大学机械工程学院, 江苏南京 210094;

<sup>2</sup>南京理工大学数控成形技术与装备国家地方联合实验室, 江苏南京 210094

**摘要** 激光粉末床熔融(LPBF)技术是近年来快速发展的一种增材制造技术, 高强铝合金具有低密度、高强度的特点, 如何使用 LPBF 技术高质量地打印高强铝合金成为近年来的研究热点。本课题组创新性地将含 Zr 的非晶合金引入到 7075 高强铝合金中, 探究了含 Zr 非晶合金对 7075 高强铝合金 LPBF 打印质量的影响。研究发现, 含 Zr 非晶合金的添加可以有效实现晶粒细化, 对于 7075 高强铝合金 LPBF 打印过程中的凝固裂纹具有明显的抑制作用。通过改变工艺参数探究了激光功率、扫描速度和扫描间距对单层单道、单层多道以及实体打印件的影响规律。通过正交试验发现致密度和显微硬度最优的工艺参数区间为激光功率 300~340 W, 扫描速度 600~800 mm/s, 扫描间距 50~70 μm, 并在激光能量密度为 142.9 J/mm<sup>3</sup> 时得到了致密度为 99.4%、显微硬度为 154.4 HV 的块体试样。本研究对于提高高强铝合金 LPBF 可打印性以获得质量稳定的无缺陷打印件具有重要意义。

**关键词** 激光技术; 激光粉末床熔融; 高强铝合金; 凝固裂纹; 微观组织

中图分类号 TG146.2+1 文献标志码 A

DOI: 10.3788/CJL202249.1402209

## 1 引言

激光粉末床熔融(LPBF)是一种新型的制造方式, 先采用软件将三维模型切层, 然后用激光逐层扫描和熔化粉末材料, 层层堆积得到三维实体<sup>[1-2]</sup>。人们研究较多的 LPBF 合金主要包括钛合金<sup>[3-5]</sup>、钴铬合金<sup>[6-7]</sup>和镍基高温合金<sup>[8-9]</sup>等, 对铝合金 LPBF 成形研究最多的是 AlSi10Mg 等 Al-Si 系合金<sup>[10-12]</sup>。以 7075 为代表的高强铝合金具有更高的硬度与强度, 在航空航天和武器装备制造等方面具有独特优势。然而, 由于高强铝合金的凝固区间较宽、打印性能较差, 在 LPBF 成形过程中易产生凝固裂纹等缺陷<sup>[13]</sup>, 严重影响了 LPBF 高强铝合金的力学性能, 限制了高强铝合金在增材制造领域的应用。因此, 研究如何提高高强铝合金的 LPBF 可打印性, 获得质量稳定的无缺陷打印件, 对于扩展增材制造的可用工程材料库具有重要意义。

目前, 人们对 7075 等高强铝合金 LPBF 成形的研究主要集中于材料改性与工艺优化两个方向。Martin 等<sup>[14]</sup>通过研究发现, 使用静电自组装工艺在 7075 铝合金中添加易于形核的 ZrH<sub>2</sub> 纳米颗粒, 可以促进新晶粒的成核, 解决该合金在 LPBF 成形过程中易产生裂纹的问题, 但该工艺易产生氢气孔且较为复杂, 不利

于工业推广。Montero-Sistiaga 等<sup>[15]</sup>研究后发现, Si 元素的引入可以抑制 7075 铝合金 LPBF 过程中凝固裂纹的产生, 在 7075 铝合金中加入适量的 Si 可以得到致密度高达 99% 且基本无裂纹的试件, 但是 Si 元素的引入会使打印件的塑性变差。Zhang 等<sup>[16]</sup>发现在 Al-Cu-Mg 合金中引入 Ti 后会在 LPBF 过程中析出 Al<sub>3</sub>Ti 相, 该相可以有效促进 Al-Cu-Mg 合金晶粒细化; 他们采用该方法得到了抗拉强度为 426.4 MPa、延伸率为 9.1% 的打印试样; 但是, 该种方法的粉末制备周期较长, 生产成本较高。

研究人员在工艺参数调整方面进行了大量研究。Stoprya 等<sup>[17]</sup>研究了 7075 铝合金 LPBF 工艺参数与缺陷之间的关系, 结果发现, 单采用工艺参数优化和热处理等方式无法完全消除凝固裂纹, 通过降低 7075 粉末中杂质 Si 的含量, 并进行基板预热, 可以提高凝固温度和减小收缩应力, 进而大幅度提高试件的抗开裂性能。Cao 等<sup>[18]</sup>研究了热输入、搭接率和激光扫描策略对 2024 铝合金 LPBF 可打印性的影响, 结果发现, 采用双向激光扫描策略可以实现 2024 铝合金的无裂纹或短裂纹 LPBF 打印。Spierings 等<sup>[19]</sup>研究了不同激光扫描速度下 Al-Mg-Sc-Zr 合金 LPBF 成形件微观组织的演变情况, 结果发现: 随着扫描速度从

收稿日期: 2021-09-14; 修回日期: 2021-10-23; 录用日期: 2021-12-13

基金项目: 国家重点研发计划(2017YFB1103000)、国家自然科学基金(51805267)

通信作者: \*liutingting@mail.njust.edu.cn

170 mm/s 增加到 350 mm/s, 细晶区域的峰值晶粒尺寸会从  $1.1 \mu\text{m}$  减小到  $600 \text{ nm}$ , 而粗晶区域的峰值晶粒尺寸基本维持不变;  $\text{Al}_3\text{Sc}$  粒子仅在低扫描速度下析出, 这是由于此时的激光能量输入较高。由以上国内外研究可知, 在高强铝合金中引入  $\text{Zr}$ 、 $\text{Sc}$ 、 $\text{Ti}$  等元素, 并进行工艺参数优化, 可以在一定程度上抑制凝固裂纹的产生, 但成形件的综合力学性能还有待进一步优化。

本研究团队创新性地将  $\text{ZrCuAlNi}$  非晶合金引入到 7075 高强铝合金中, 实现了 7075 高强铝合金 LPBF 打印过程中凝固裂纹的抑制和消除, 得到了无裂纹、高硬度的 LPBF 成形试样。该方法为抑制和消除高强铝合金 LPBF 过程中产生的凝固裂纹以及细化晶粒组织和强化成形件的力学性能等提供了一种全新的有效途径。

## 2 试验材料、设备及方法

### 2.1 材料与设备

非晶合金的化学式为  $\text{Zr}_{50.7}\text{Cu}_{28}\text{Al}_{12.3}\text{Ni}_9$ , 7075

铝合金粉末的化学成分见表 1。将适量  $\text{ZrCuAlNi}$  非晶合金粉末加入到 7075 高强铝合金粉末中, 混合粉末中  $\text{ZrCuAlNi}$  的质量分数为 8%, 然后使用 V 型混粉机在高纯氩气保护条件下机械混粉 48 h, 混粉机转速为 20 r/min, 得到改性后的复合粉末。使用 Mastersizer 3000 激光粒度分析仪对复合粉末进行分析测试, 得到粉末的粒径分布。复合粉末的形貌及粒径分布如图 1 所示。

表 1 7075 铝合金粉末的化学成分

Table 1 Chemical composition of 7075 aluminum alloy powder

| Element | Mass fraction / % |
|---------|-------------------|
| Al      | Bal.              |
| Zn      | 5.84              |
| Mg      | 2.28              |
| Cu      | 1.71              |
| Fe      | 0.06              |
| Si      | 0.18              |
| Cr      | 0.19              |
| Ti      | 0.03              |

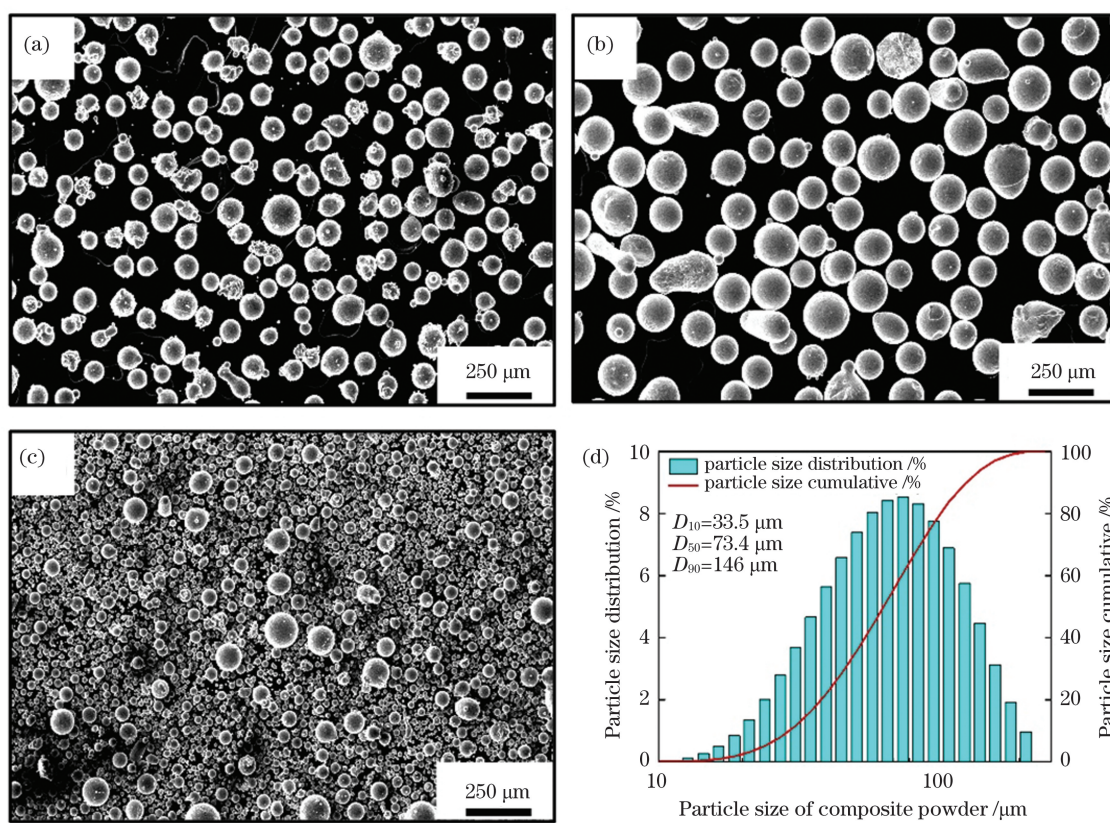


图 1 粉末形貌及粒径分布。(a)7075 铝合金粉末;(b) $\text{ZrCuAlNi}$  非晶合金粉末;(c)复合粉末;(d)复合粉末的粒径分布

Fig. 1 Morphologies and particle size distribution of powders. (a) 7075 aluminum alloy powder; (b)  $\text{ZrCuAlNi}$  amorphous alloy powder; (c) composite powder; (d) particle size distribution of composite powder

LPBF 试验采用 Concept Laser 公司生产的 M2 金属打印机进行, 该打印机配备 400 W 单模连续光纤激光器, 激光波长为 1070 nm, 光斑尺寸为  $80 \mu\text{m}$ , 最大成形尺寸为  $250 \text{ mm} \times 250 \text{ mm} \times 280 \text{ mm}$ 。为避免打印过程中金属粉末与氧气反应, 通入体积分数为

99.99% 的氩气作为保护气体, 以保证成形腔内氧气的体积分数始终不超过 0.1%。

### 2.2 工艺参数

设计了单层单道、单层多道 LPBF 打印工艺参数, 试验参数见表 2。其中,  $E$  为激光能量密度,  $P$  为激光

功率,  $v$  为扫描速度,  $H$  为扫描间距,  $t$  为铺粉层厚。设计正交试验, 对块体试样进行打印, 试验参数见表 3, 扫描策略为 45° 蛇形扫描, 相邻层间扫描方向旋转 90°。激光能量密度的计算公式为

$$E = \frac{P}{Hvt} \quad (1)$$

表 2 单层单道和单层多道打印参数

Table 2 LPBF process parameters of single-track and multi-track

| Print mode   | $P$ / W            | $v$ / (mm·s <sup>-1</sup> )    | $t$ / $\mu\text{m}$ | $H$ / $\mu\text{m}$ | $E$ / (J·mm <sup>-3</sup> ) |
|--------------|--------------------|--------------------------------|---------------------|---------------------|-----------------------------|
| Single-track | 260, 300, 340, 380 | 200, 400, 600, 800, 1000, 1200 | 70                  |                     |                             |
| Multi-track  | 380                | 400, 600, 800, 1000            | 70                  | 50, 70, 90, 110     | 49.4~271.4                  |

表 3 正交试验打印参数

Table 3 Orthogonal experiment process parameters

| Sample | Laser power / W | Scanning speed / (mm·s <sup>-1</sup> ) | Hatch distance / $\mu\text{m}$ | Layer thickness / $\mu\text{m}$ |
|--------|-----------------|--|--------------------------------|---------------------------------|
| S1     |                 | 400                                    | 50                             | 70                              |
| S2     | 260             | 600                                    | 70                             | 70                              |
| S3     |                 | 800                                    | 90                             | 70                              |
| S4     |                 | 1000                                   | 110                            | 70                              |
| S5     |                 | 400                                    | 70                             | 70                              |
| S6     | 300             | 600                                    | 50                             | 70                              |
| S7     |                 | 800                                    | 110                            | 70                              |
| S8     |                 | 1000                                   | 90                             | 70                              |
| S9     |                 | 400                                    | 90                             | 70                              |
| S10    | 340             | 600                                    | 110                            | 70                              |
| S11    |                 | 800                                    | 50                             | 70                              |
| S12    |                 | 1000                                   | 70                             | 70                              |
| S13    |                 | 400                                    | 110                            | 70                              |
| S14    | 380             | 600                                    | 90                             | 70                              |
| S15    |                 | 800                                    | 70                             | 70                              |
| S16    |                 | 1000                                   | 50                             | 70                              |

### 2.3 测试方法

打印完成后, 使用金属线切割机将打印件从基板上割下, 然后将所有打印件置于无水乙醇中超声清洗 30 min, 以清除打印件表面的污垢。使用砂纸和抛光布对打印件进行打磨抛光, 接着用 Keller 试剂 (190 mL H<sub>2</sub>O + 5 mL HNO<sub>3</sub> + 3 mL HCl + 2 mL HF) 对打印件进行腐蚀, 腐蚀时间为 7 s, 然后使用阿基米德排水法和金相图片法分别对块体试样进行致密度测量。使用 VK-X100 激光共聚焦显微镜和 FEI Quananta 250F 扫描电子显微镜观测打印件的形貌, 采用电子背散射衍射(EBSD)技术对块体试样的晶粒尺寸和晶粒取向进行测量。使用显微硬度仪对抛磨后的块体试样进行显微硬度测试, 每个试样沿对角线方向取 10 个点, 测试所用载荷为 49.03 N, 加载时间为 15 s。

## 3 单道与多道试验结果分析

### 3.1 单道打印结果分析

稳定的单道打印是实现高质量单层打印和块体

打印的基础。图 2 所示是不同工艺参数下单道熔道的表面形貌, 可以看出, 在低激光功率和高扫描速度下, 熔道的连续性较差, 部分区域的熔道尺寸突然增大或减小。随着激光扫描速度减小和激光功率增大, 粉末吸收的能量增多, 产生了更多的熔融态金属, 液态熔池存在的时间更长<sup>[20]</sup>, 最终成形出更宽的单道熔池, 熔道的稳定性也更好。但是, 随着激光功率继续增大和激光扫描速度继续减小, 能量输入增大, 熔道出现了较为明显的“凝固波纹”形貌<sup>[10]</sup>, 导致熔道的平整性变差。

单道熔池的横截面形貌如图 3 所示, 随着激光扫描速度从 400 mm/s 增大到 1000 mm/s, 熔池的深度逐渐减小。激光扫描速度对熔池的熔化模式具有显著影响, 过低的扫描速度易在熔池底部产生匙孔, 而过高的激光扫描速度由于激光能量不足, 产生的熔池较小, 易产生未熔合孔洞等缺陷。当激光功率为 380 W 时, 600~800 mm/s 是较为合适的扫描速度区间。

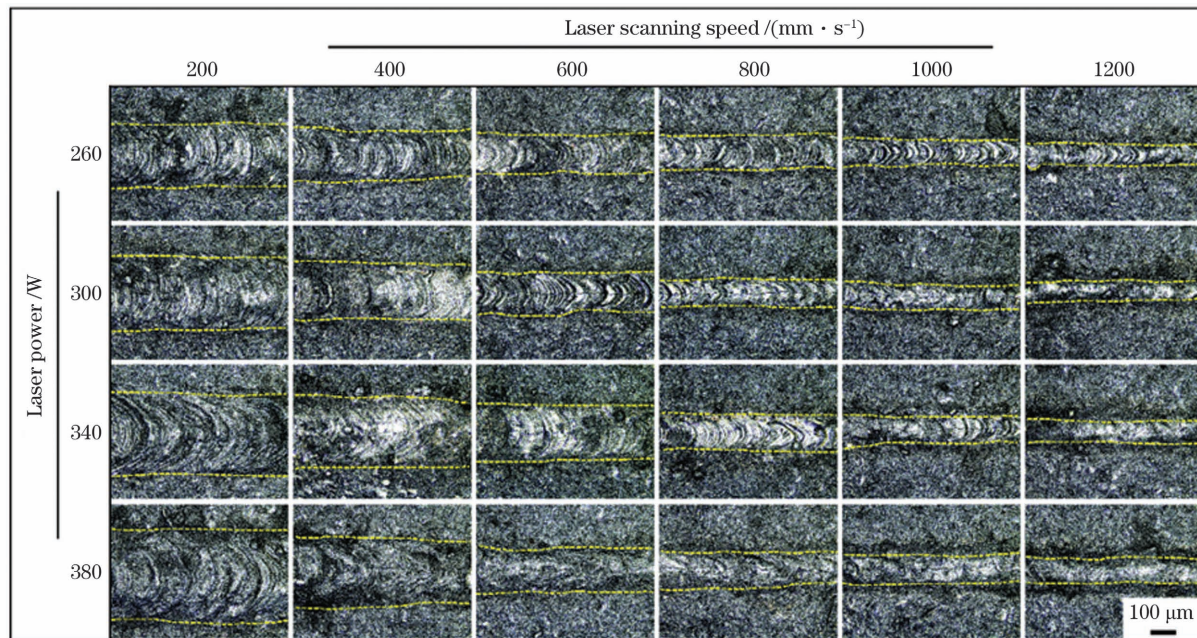


图2 不同打印参数下单道熔道的表面形貌

Fig. 2 Surface morphologies of single-track under different process parameters

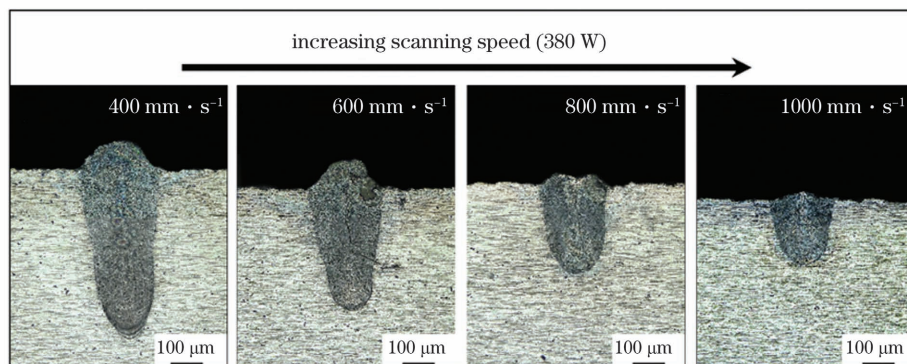


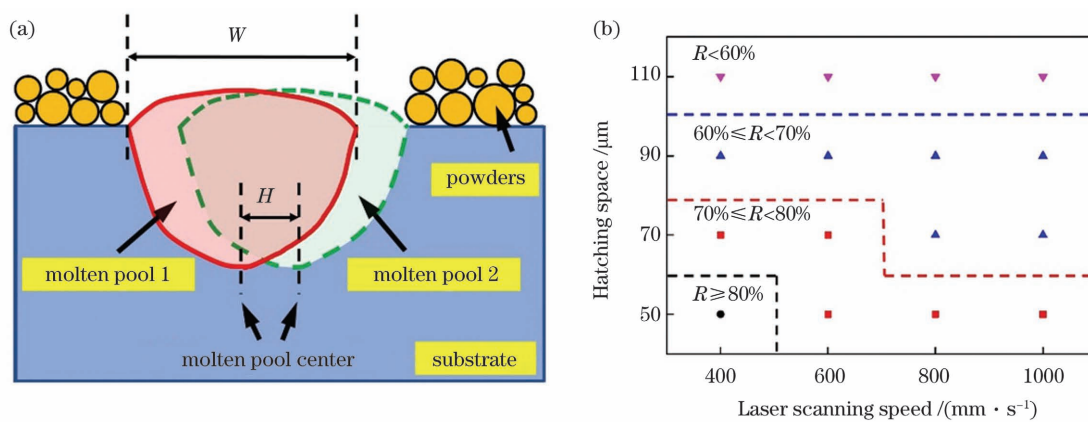
图3 不同激光扫描速度下单道熔池的截面形貌(380 W)

Fig. 3 Cross-section morphologies of single-track molten pool under different laser scanning speeds (380 W)

### 3.2 多道打印结果分析

激光扫描间距通过影响相邻两个熔道之间的重叠面积来影响单层打印质量,而由于激光功率和扫描速度都会对单道熔道的宽度产生影响,所以可将相邻熔道重叠面积这一影响指标转换成搭接率来进行分析。

搭接率能够反映多道打印过程中熔道与熔道之间的重叠程度,是影响LPBF打印试样表面质量的重要因素之一,可以通过计算相邻熔池间的中心距离得到,如图4(a)所示。图4(a)中,W表示熔池宽度,H表示激光扫描间距。搭接率R的计算公式为

图4 熔道搭接示意图以及不同工艺参数下熔道搭接率的统计图( $P=380\text{ W}$ )。(a)熔道搭接示意图;(b)搭接率统计图Fig. 4 Schematic of track overlap and statistical diagram of track overlap rate under different process parameters ( $P=380\text{ W}$ ).

(a) Schematic of track overlap; (b) statistical diagram of track overlap rate

$$R = \frac{W - H}{W}。 \quad (2)$$

通过计算,可以得到不同工艺参数下单层多道熔道的搭接率,如图 4(b)所示。

搭接率的大小会影响单层打印的表面质量,从图 5 所示的单层打印三维形貌图中可以看到,随着扫描间距增大,熔道搭接率逐渐减小。当搭接率达到 80% 时,如图 5(a)所示,较高的搭接率使得前面已经凝固成形的熔道因激光再次作用发生重熔,重熔部位的金属熔体会黏附相邻尚未熔化的合金粉末,凝固后易出现凸起,而新熔道上熔化的金属粉末较少,熔池不均匀性增大,可能产生凹坑等缺陷,导致整体表面不够平整。当搭接率小于 60% 时,如图 5(d)所示,相邻熔道之间搭接不够,熔道与熔道之间分隔明显,导致表面质量较差。适当的搭接率可以在保证熔道连续性的同

时起到重熔上一熔道、预热下一熔道的作用<sup>[21]</sup>,有利于得到稳定且成形质量较好的单层打印样件。结合图 4(b)和图 5 可以发现,当搭接率在 60%~80% 范围内时,可以得到较为稳定的单层表面成形质量,平均表面粗糙度低于 13 μm。

实体件属于多层多道打印结构,单层打印质量的好坏会影响实体打印件的打印质量,稳定较好的单层表面质量可使下一层的铺粉更加均匀,可以降低实体的内部缺陷,提高实体打印件的成形质量。综上所述,既要选择合适的激光功率和扫描速度,也要选择合适的扫描间距,以及设计适中的熔道搭接率,这样才能保证复合粉末吸收足够的能量从而形成充足的金属熔体,同时保证熔融金属有足够的流动扩散,得到较平整的表面,最终得到高致密度、无裂纹的打印实体。

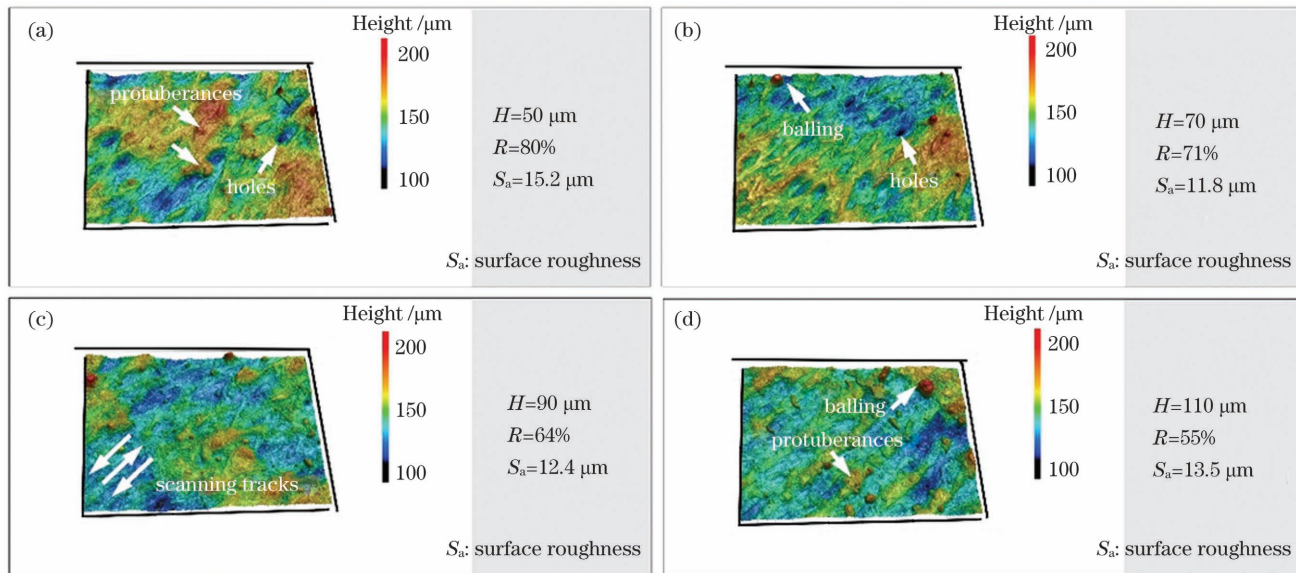


图 5 不同工艺参数下的三维表面形貌

Fig. 5 Three-dimensional surface morphologies under different process parameters

## 4 块体试样打印结果分析

### 4.1 致密度分析

正交试验参数下打印块体试样的截面形貌如图 6 所示。正交试验方差分析(表 4)表明,激光扫描速度的改变对块体试样的致密度有显著影响。在本试验研究参数范围内,激光扫描速度是影响致密度的最主要因素。激光功率的大小主要对孔隙缺陷的数量产生影响:随着激光功率从 260 W 增大到 340 W,孔隙缺陷的数量呈减少的趋势;之后随着激光功率继续增大到 380 W,孔隙缺陷的数量逐渐增加。扫描速度的大小主要对孔隙缺陷的类型产生影响:随着扫描速度从 1000 mm/s 减小到 400 mm/s,孔隙缺陷逐渐从以未熔合孔隙缺陷为主转变成以气孔缺陷为主。

试样 S1 是在较大激光能量密度下成形的,部分熔池底部出现了匙孔缺陷,如图 7(a)所示;同时,较高的

能量输入也提高了熔池温度,促进了低熔点合金元素的蒸发,加速了熔池中气孔的扩展和生长,在熔池中形成了一些大小不一的球形气孔。试样 S4 是在过低的激光能量密度下成形的,部分复合粉末未完全熔化,形成了一些以熔池壁为边缘、形状不规则的未熔合孔隙缺陷,如图 7(b)所示,严重降低了成形试样的致密度。如图 7(c)所示,试样 S6 的成形质量最好,内部未见孔隙缺陷,致密度最高。对于试样 S13,高的激光功率和低的扫描速度使得上一层产生的匙孔可能被下一层激光扫描破坏并重新熔合,因而在部分熔池底部产生较大的匙孔缺陷,如图 7(d)所示。此外,相对较高的能量输入也促进了熔池中熔体的流动,延长了熔池的成形时间,可以促进熔池内部气体的逸出<sup>[22]</sup>,因此微型气孔数量减少。

图 8 为激光功率和扫描速度对块体试样致密度的影响。可以看到,试样的致密度随着激光功率和扫描速

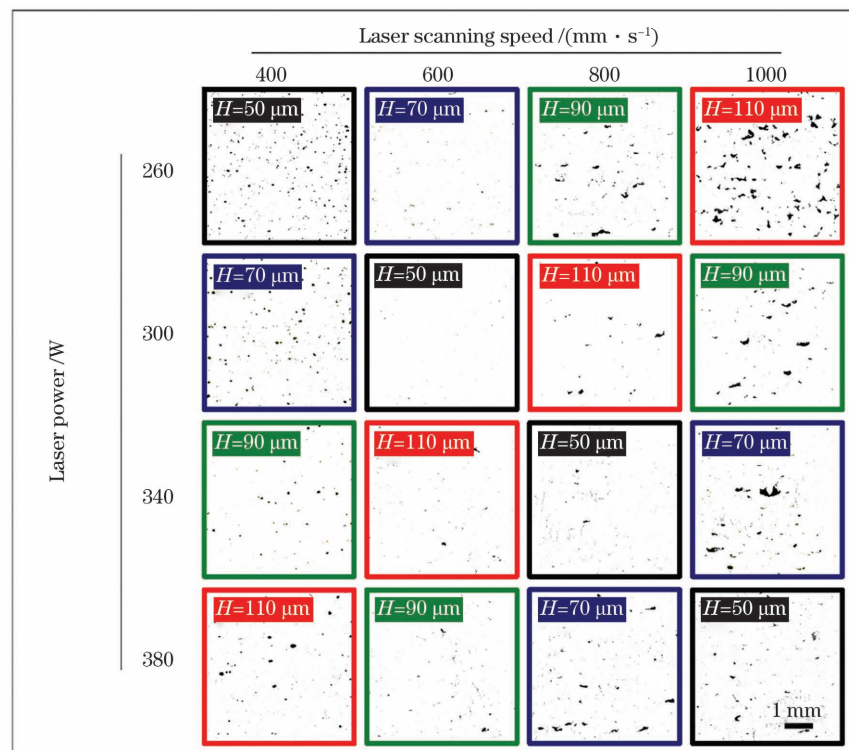


图 6 正交试验参数下打印块体试样截面拼接图

Fig. 6 Stitched image of cubic specimens printed under different orthogonal experiment parameters

表 4 正交试验方差分析表

Table 4 Analysis of variance of orthogonal experiment

| Factor               | Sum of squares | Degree of freedom | Mean squares | F      | Significance |
|----------------------|----------------|-------------------|--------------|--------|--------------|
| Laser power          | 0.000483       | 3                 | 0.000161     | 2.3139 |              |
| Laser scanning speed | 0.000888       | 3                 | 0.000296     | 4.2544 | *            |
| Hatch distance       | 0.000096       | 3                 | 0.000032     | 0.4601 |              |
| Error                | 0.000418       | 6                 | 0.000070     |        |              |
| Total error          | 0.001885       | 15                |              |        |              |

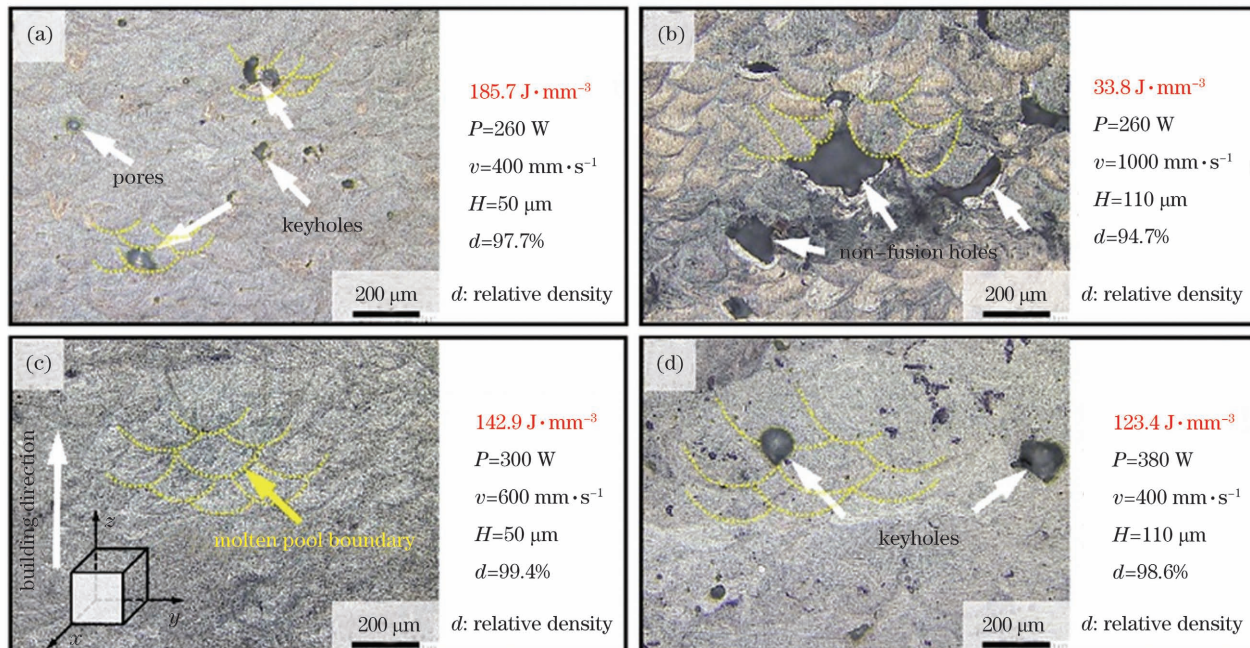


图 7 块体试样的金相图。(a)试样 S1;(b)试样 S4;(c)试样 S6;(d)试样 S13

Fig. 7 Metallographic diagrams of cubic samples. (a) Sample S1; (b) sample S4; (c) sample S6; (d) sample S13

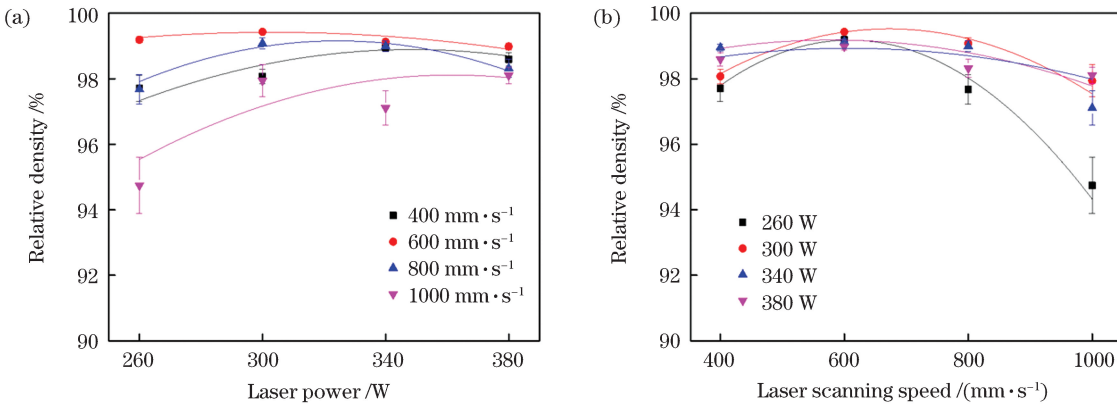


图 8 激光功率和扫描速度对致密度的影响。(a)激光功率对致密度的影响;(b)激光扫描速度对致密度的影响

Fig. 8 Influences of laser power and scanning speed on relative density. (a) Influence of laser power on relative density; (b) influence of laser scanning speed on relative density

度的增加呈现先增后减的变化趋势。综合正交试验分析结果,最终可以得到致密度最优的工艺参数区间为: $P=300\sim340\text{ W}$ , $v=600\sim800\text{ mm/s}$ , $H=50\sim70\text{ }\mu\text{m}$ 。

#### 4.2 微观组织分析

激光能量密度的大小会影响熔池组织的生长方式与晶粒形态。图 9 给出了块体试样 S4 和 S6 的扫描电镜(SEM)图。试样 S4 的激光能量输入较低,溶质分散不均匀, $\text{Al}_3\text{Zr}$  等粒子优先在凝固前沿产生,聚集在熔池底部<sup>[23]</sup>,由于  $\text{Al}_3\text{Zr}$  粒子的形核作用,熔池底部的晶粒组织较为细小<sup>[24]</sup>。熔池底部偏上的晶体组织沿着温度梯度方向择优生长,形成较粗大的树枝状组织,如图 9(a-3)所示,未凝固的金属熔体会填充进这些树枝状晶体组织中间,一些狭长的晶枝间区域难以得

到有效填充,形成了狭长的晶枝间隙。填充在晶枝间的金属熔体在凝固过程中会由于热收缩而产生垂直于晶界方向的残余拉应力<sup>[25]</sup>,当这些长条形的晶体组织无法抵消拉应力而发生断裂时,狭长的晶枝间隙便为裂纹扩展提供了通道,最终形成了沿着温度梯度方向扩展的凝固裂纹,如图 10(a)所示;这些凝固裂纹会沿着晶界扩展,有时甚至跨越多个熔池,会严重影响高强铝合金 LPBF 成形试样的力学性能<sup>[26]</sup>。随着激光能量输入的增加,熔池温度升高,熔池的扩散和溶质再分布得到改善<sup>[27]</sup>,有利于  $\text{Al}_3\text{Zr}$  粒子的形成,从而大大增加了熔池中的形核位点数,实现多点形核,最终得到显微组织均匀且细小的等轴晶(平均晶粒尺寸只有 $1\sim2\text{ }\mu\text{m}$ ),如图 9(b-3)所示。

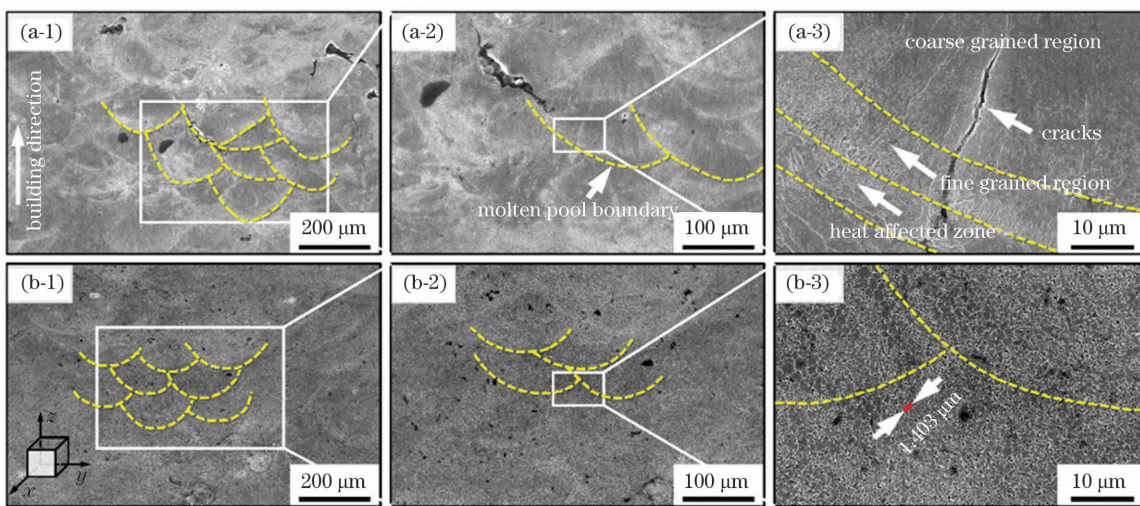


图 9 块体试样的 SEM 图像。(a)试样 S4;(b)试样 S6

Fig. 9 SEM images of cubic samples. (a) Sample S4; (b) sample S6

图 11(a)、(b)为块体试样 S6 的电子背散射衍射(EBSD)取向图和极图。试样 S6 的 EBSD 取向图显示晶粒组织全部为细小的等轴晶,EBSD 极图显示这些晶粒取向为各向同性,未表现出强的织构方向。相对于柱状晶而言,等轴晶更容易旋转和变形,以释放应力<sup>[15]</sup>,从而可以抵消熔池凝固过程中产生的残余拉应

力,如图 10(b)所示。未改性 7075 铝合金 LPBF 试样的晶粒组织以柱状晶为主,如图 11(c)所示,该试样内部可见许多沿着柱状晶生长方向分布的裂纹<sup>[14]</sup>。2024 高强铝合金 LPBF 单道熔池的凝固裂纹扩展情况如图 11(d)所示<sup>[18]</sup>,可以发现,凝固裂纹的分布和扩展方式在很大程度上取决于熔池凝固过程中产生的晶

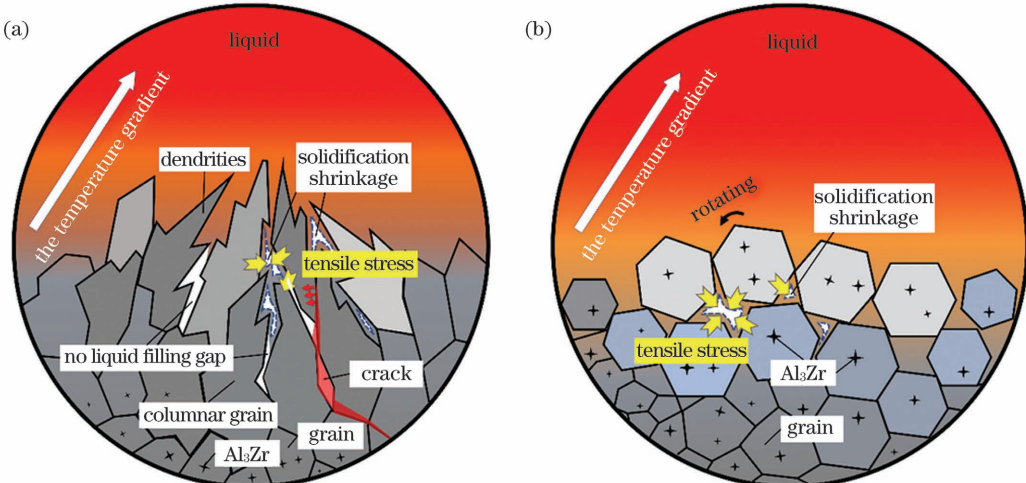
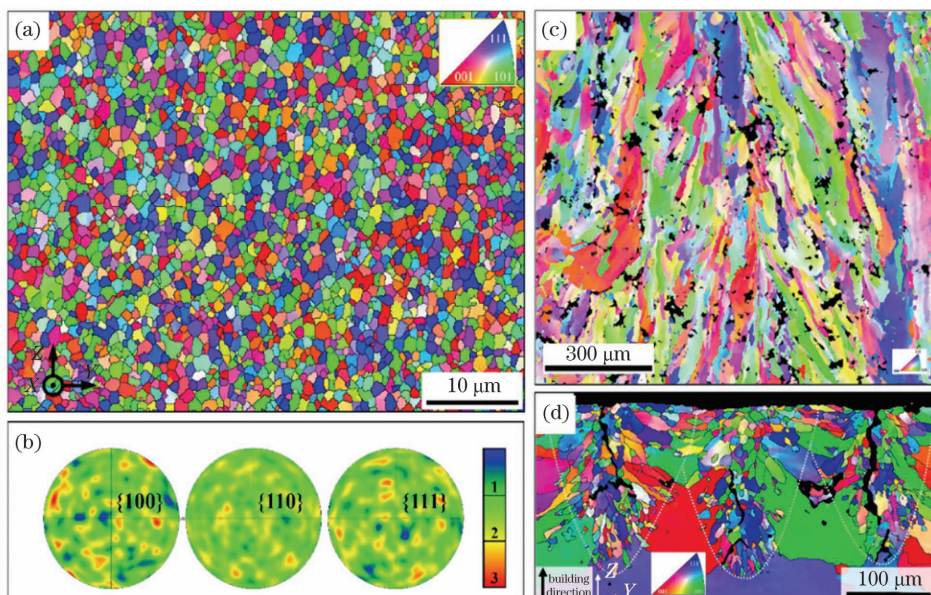


图 10 柱状晶和等轴晶的结构示意图。(a)柱状晶;(b)等轴晶

Fig. 10 Structure diagrams of columnar and equiaxed grains. (a) Columnar grains; (b) equiaxed grains

图 11 EBSD 分析。(a)S6 试样的 EBSD 取向图;(b)S6 试样的极图;(c) 7075 合金 LPBF 成形试样的 EBSD 表征图<sup>[14]</sup>;(d) 2024 合金单层三道 LPBF 成形试样的 EBSD 表征图<sup>[18]</sup>Fig. 11 Electron back-scatter diffraction (EBSD) analysis. (a) Grain orientation map of sample S6; (b) pole figures of sample S6; (c) EBSD characterization of 7075 aluminum alloy LPBF forming sample<sup>[14]</sup>; (d) EBSD characterization of 2024 aluminum alloy single-layer three-track LPBF forming sample<sup>[18]</sup>

粒组织,单道熔池由于没有后续的热量补充,更容易产生凝固裂纹,以释放残余应力。对比未改性 7075 高强铝合金的 LPBF 试验结果<sup>[14,28]</sup>可以发现,引入含 Zr 的非晶合金后,在适当的工艺参数下能够通过细化晶粒实现 7075 铝合金 LPBF 过程中凝固裂纹的抑制和消除。

#### 4.3 硬度分析

图 12 所示是块体试样致密度随激光能量密度的变化曲线,试样的平均显微硬度随着激光能量密度的增大呈现增大的趋势,最大平均硬度达到 154.4 HV。对正交试验得到的显微硬度测试结果进行极差分析和方差分析可知,激光扫描速度是影响块体试样显微硬度的最主要因素。在较低的激光扫描速度和相对较高的激光能量密度下可以得到更高的显微硬度,显微硬度的最优工艺参数区间与致密度的最优工艺参数区间重合。

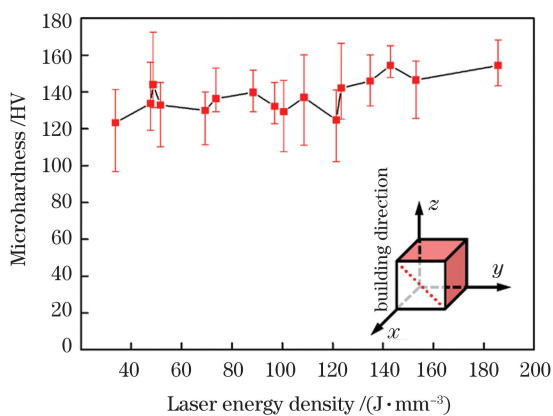


图 12 激光能量密度对块体试样显微硬度的影响

Fig. 12 Influence of laser energy density on microhardness of cubic samples

金属零件的硬度通常与微观晶粒尺寸、析出相有关<sup>[29]</sup>。含 Zr 非晶合金的引入,一方面通过晶粒细化提升了打印件的力学性能,另一方面,非晶合金本身具有高强度、高硬度的特点,大大增强了 7075 高强铝合金 LPBF 打印件的硬度值。图 13 所示为本文和部分文献中 7075 高强铝合金 LPBF 成形试样的显微硬度比较,可以发现,本文 7075 高强铝合金 LPBF 试样的硬度值明显高于未引入其他元素且未经过任何热处理的试样,与未添加 Si 元素的 7075 高强铝合金 LPBF 成形试样<sup>[15]</sup>相比,硬度值提升了 17.7%,达到了进行固溶热处理+两次时效处理(SHT+AA+AA)后的水平<sup>[30]</sup>。

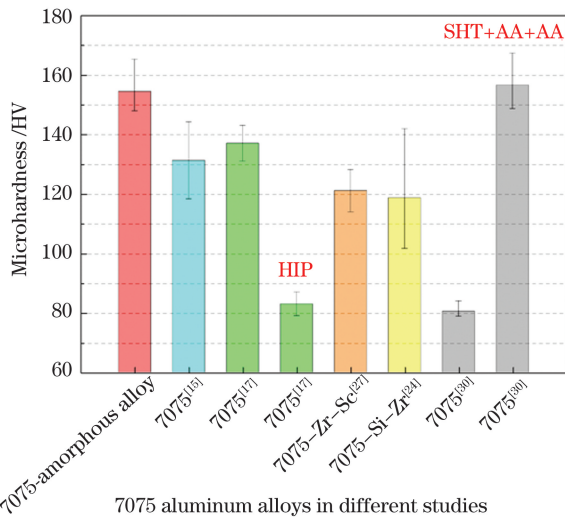


图 13 LPBF 成形 7075 铝合金试样显微硬度(HIP:热等静压)

Fig. 13 Microhardness of 7075 aluminum alloys fabricated by LPBF (HIP: hot isostatic pressing)

## 5 结 论

本研究面向高强铝合金的 LPBF 可打印性提升与质量控制,创新性地将含 Zr 的非晶合金引入到 7075 高强铝合金中,研究了不同工艺条件下含 Zr 非晶合金对 7075 高强铝合金打印质量的影响。主要得出以下结论:

1) 含 Zr 非晶合金的引入可以实现 7075 高强铝合金 LPBF 打印过程中的晶粒细化,对于凝固裂纹具有明显的抑制作用。随着激光能量密度从 33.8 J/mm<sup>3</sup>增大到 142.9 J/mm<sup>3</sup>,熔池晶粒组织逐渐转变成细小的等轴晶,晶粒尺寸只有 1~2 μm,实现了完全的晶粒细化,得到了致密度达 99.4% 的无裂纹成形试样。

2) 非晶合金的引入可以优化 7075 铝合金 LPBF 打印件的力学性能,沉积态试样的硬度值达到 154.4 HV,与未改性的 7075 铝合金 LPBF 打印件相比,硬度值提升 17.7%。正交试验结果表明,最高致密度和最大显微硬度的工艺区间重合,最优工艺参数区间为:激光功率 300~340 W,激光扫描速度 600~

800 mm/s,激光扫描间距 50~70 μm。

3) 对单道熔道进行分析后发现,激光功率与激光扫描速度会影响单道熔池的尺寸与形貌,过高或过低的激光功率与激光扫描速度均不利于稳定熔道的形成。分析单层打印表面粗糙度可以发现,激光扫描间距的大小也会影响单层表面成形质量,搭接率为 60%~80% 时可以得到表面粗糙度低于 13 μm 的单层表面打印质量。

## 参 考 文 献

- [1] DebRoy T, Wei H L, Zuback J S, et al. Additive manufacturing of metallic components—process, structure and properties [J]. Progress in Materials Science, 2018, 92: 112-224.
- [2] Wang P, Eckert J, Prashanth K G, et al. A review of particulate-reinforced aluminum matrix composites fabricated by selective laser melting [J]. Transactions of Nonferrous Metals Society of China, 2020, 30(8): 2001-2034.
- [3] Wei H L, Cao Y, Liao W H, et al. Mechanisms on inter-track void formation and phase transformation during laser powder bed fusion of Ti-6Al-4V [J]. Additive Manufacturing, 2020, 34: 101221.
- [4] Machirori T, Liu F Q, Yin Q Y, et al. Spatiotemporal variations of residual stresses during multi-track and multi-layer deposition for laser powder bed fusion of Ti-6Al-4V [J]. Computational Materials Science, 2021, 195: 110462.
- [5] 钦兰云, 门继华, 赵朔, 等. TiB<sub>2</sub> 含量对选区激光熔化 TiB/Ti-6Al-4V 复合材料组织及力学性能的影响 [J]. 中国激光, 2021, 48(6): 0602102.
- [6] Qin L Y, Men J H, Zhao S, et al. Effect of TiB<sub>2</sub> content on microstructure and mechanical properties of TiB/Ti-6Al-4V composites formed by selective laser melting [J]. Chinese Journal of Lasers, 2021, 48(6): 0602102.
- [7] Tonelli L, Fortunato A, Ceschin L. CoCr alloy processed by selective laser melting (SLM): effect of laser energy density on microstructure, surface morphology, and hardness [J]. Journal of Manufacturing Processes, 2020, 52: 106-119.
- [8] Gu Z, Su X, Peng W S, et al. An important improvement of strength and ductility on a new type of CoCr<sub>2.5</sub>FeNi<sub>2</sub>TiW<sub>0.5</sub> high entropy alloys under two different protective gases by selective laser melting [J]. Journal of Alloys and Compounds, 2021, 868: 159088.
- [9] Wei H L, Knapp G L, Mukherjee T, et al. Three-dimensional grain growth during multi-layer printing of a nickel-based alloy Inconel 718 [J]. Additive Manufacturing, 2019, 25: 448-459.
- [10] 潘爱琼, 张辉, 王泽敏. 镍基单晶高温合金选区激光熔化成形工艺及组织 [J]. 中国激光, 2019, 46(11): 1102007.
- [11] Pan A Q, Zhang H, Wang Z M. Process parameters and microstructure of Ni-based single crystal superalloy processed by selective laser melting [J]. Chinese Journal of Lasers, 2019, 46(11): 1102007.
- [12] Yang T, Liu T T, Liao W H, et al. The influence of process parameters on vertical surface roughness of the AlSi10Mg parts fabricated by selective laser melting [J]. Journal of Materials Processing Technology, 2019, 266: 26-36.
- [13] Xiao Y K, Yang Q, Bian Z Y, et al. Microstructure, heat treatment and mechanical properties of TiB<sub>2</sub>/Al-7Si-Cu-Mg alloy fabricated by selective laser melting [J]. Materials Science and Engineering A, 2021, 809: 140951.
- [14] Jiang L Y, Liu T T, Zhang C D, et al. Preparation and mechanical properties of CNTs-AlSi10Mg composite fabricated via selective laser melting [J]. Materials Science and Engineering A, 2018, 734: 171-177.
- [15] Aboulkhair N T, Simonelli M, Parry L, et al. 3D printing of aluminium alloys: additive manufacturing of aluminium alloys

- using selective laser melting[J]. Progress in Materials Science, 2019, 106: 100578.
- [14] Martin J H, Yahata B D, Hundley J M, et al. 3D printing of high-strength aluminium alloys[J]. Nature, 2017, 549(7672): 365-369.
- [15] Montero-Sistiaga M L, Mertens R, Vrancken B, et al. Changing the alloy composition of Al7075 for better processability by selective laser melting[J]. Journal of Materials Processing Technology, 2016, 238: 437-445.
- [16] Zhang J L, Gao J B, Song B, et al. A novel crack-free Ti-modified Al-Cu-Mg alloy designed for selective laser melting[J]. Additive Manufacturing, 2021, 38: 101829.
- [17] Stoprya W, Gruber K, Smolina I, et al. Laser powder bed fusion of AA7075 alloy: influence of process parameters on porosity and hot cracking[J]. Additive Manufacturing, 2020, 35: 101270.
- [18] Cao Y, Wei H L, Yang T, et al. Printability assessment with porosity and solidification cracking susceptibilities for a high strength aluminum alloy during laser powder bed fusion [J]. Additive Manufacturing, 2021, 46: 102103.
- [19] Spierings A B, Dawson K, Uggowitzer P J, et al. Influence of SLM scan-speed on microstructure, precipitation of  $\text{Al}_3\text{Sc}$  particles and mechanical properties in Sc- and Zr-modified Al-Mg alloys[J]. Materials & Design, 2018, 140: 134-143.
- [20] Wei P, Wei Z Y, Chen Z, et al. The AlSi10Mg samples produced by selective laser melting: single track, densification, microstructure and mechanical behavior [J]. Applied Surface Science, 2017, 408: 38-50.
- [21] Tian Y, Tomus D, Rometsch P, et al. Influences of processing parameters on surface roughness of Hastelloy X produced by selective laser melting[J]. Additive Manufacturing, 2017, 13: 103-112.
- [22] Tan Q Y, Liu Y G, Fan Z Q, et al. Effect of processing parameters on the densification of an additively manufactured 2024 Al alloy[J]. Journal of Materials Science & Technology, 2020, 36(10): 1000-1005.
- [23] Griffiths S, Rossell M D, Croteau J, et al. Effect of laser rescanning on the grain microstructure of a selective laser melted Al-Mg-Zr alloy[J]. Materials Characterization, 2018, 143: 34-42.
- [24] Li L B, Li R D, Yuan T C, et al. Microstructures and tensile properties of a selective laser melted Al-Zn-Mg-Cu (Al7075) alloy by Si and Zr microalloying [J]. Materials Science and Engineering A, 2020, 787: 139492.
- [25] Li R D, Wang M B, Li Z M, et al. Developing a high-strength Al-Mg-Si-Sc-Zr alloy for selective laser melting: crack-inhibiting and multiple strengthening mechanisms [J]. Acta Materialia, 2020, 193: 83-98.
- [26] Nie X J, Zhang H, Zhu H H, et al. Effect of Zr content on formability, microstructure and mechanical properties of selective laser melted Zr modified Al-4.24Cu-1.97Mg-0.56Mn alloys[J]. Journal of Alloys and Compounds, 2018, 764: 977-986.
- [27] Lei Z L, Bi J, Chen Y B, et al. Effect of energy density on formability, microstructure and micro-hardness of selective laser melted Sc- and Zr-modified 7075 aluminum alloy[J]. Powder Technology, 2019, 356: 594-606.
- [28] 万达远, 李小强, 赖佳明, 等. 基于选择性激光熔化技术7075铝合金组织性能与裂纹的研究[J]. 应用激光, 2019, 39(1): 1-8.
- Wan D Y, Li X Q, Lai J M, et al. Microstructure properties and crack of 7075 aluminum alloy based on selective laser melting technology[J]. Applied Laser, 2019, 39(1): 1-8.
- [29] Liu J, Yao P, Zhao N Q, et al. Effect of minor Sc and Zr on recrystallization behavior and mechanical properties of novel Al-Zn-Mg-Cu alloys[J]. Journal of Alloys and Compounds, 2016, 657: 717-725.
- [30] Sun S Y, Liu P, Hu J Y, et al. Effect of solid solution plus double aging on microstructural characterization of 7075 Al alloys fabricated by selective laser melting (SLM)[J]. Optics & Laser Technology, 2019, 114: 158-163.

## Solidification Crack Elimination and Quality Control of High-Strength Aluminum Alloy 7075 Fabricated Using Laser Powder Bed Fusion

Lü Xinrui<sup>1,2</sup>, Liu Tingting<sup>1,2\*</sup>, Liao Wenhe<sup>1,2</sup>, Wei Huiliang<sup>1,2</sup>, Yang Tao<sup>1,2</sup>, Jiang Liyi<sup>1,2</sup>

<sup>1</sup> School of Mechanical Engineering, Nanjing University of Science and Technology, Nanjing 210094, Jiangsu, China;

<sup>2</sup> National Joint Engineering Laboratory for Numerical Control Forming Technology and Equipment,

Nanjing University of Science and Technology, Nanjing 210094, Jiangsu, China

### Abstract

**Objective** Laser powder bed fusion (LPBF) technology is a new type of manufacturing method. The three-dimensional (3D) model is sliced using a software, and then, powder is scanned and melted layer-by-layer using laser to obtain a 3D entity. The most studied LPBF alloys mainly include titanium alloys, cobalt-chromium alloys, and nickel-based superalloys. Meanwhile, the most studied LPBF formed aluminum alloys are Al-Si alloys, such as AlSi10Mg. High-strength aluminum alloys represented by 7075 have high hardness and strength and have unique advantages in aerospace and weapon manufacturing industries. However, the wide solidification interval of high-strength aluminum alloys and poor welding performance, defects, such as solidification cracks during the LPBF process, significantly affect the mechanical properties of the LPBF high-strength aluminum alloys, and thus restrict their application in the additive manufacturing field. Current research on the LPBF forming of high-strength aluminum alloys, such as 7075, mainly focuses on material modification and process optimization. This study explores the effect of a Zr-containing amorphous alloy on the forming quality of 7075 high-strength LPBF aluminum alloy. A printed workpiece with stable quality without cracks and defects was obtained. Our study can improve the LPBF printability of high-strength aluminum alloys and promote the expansion of the available engineering material library and process parameter library for additive manufacturing.

**Methods** The Zr-containing amorphous and 7075 high-strength aluminum alloys powders were uniformly mixed in a mass ratio of 2:23 through mechanical powder mixing to obtain composite powder. First, a single-track printing experiment was performed to explore the effects of laser power and scanning speed on the morphology of the single-track channel and the size of the molten pool. Then, a single-layer printing experiment was performed to measure the surface roughness of the printed single-layer and study the effects of the hatch distance on surface quality. Finally, the optimal combination of laser power, scanning speed, and scanning distance was explored by designing an orthogonal experiment with three factors and four levels. The Archimedes drainage and metallographic image methods were used to measure the density. Scanning electron microscope and electron backscatter diffraction technology were employed to study the effect of Zr-containing amorphous alloy on the microstructure of 7075 high-strength aluminum alloy LPBF-formed samples. In addition, the microhardness of the LPBF-formed samples under different process parameters was investigated to characterize their mechanical properties.

**Results and Discussions** This study reveals that the addition of Zr-containing amorphous alloys can effectively achieve grain refinement and has a significant inhibitory effect on solidification cracks in the LPBF printing process of 7075 high-strength aluminum alloy. Orthogonal experiment analysis results show that the change of the laser scanning speed significantly affects the density of the bulk sample, which is a crucial factor affecting the density within the range of the parameters studied in this experiment (Table 4). The optimal process parameters are laser power: 300–340 W, scanning speed: 600–800 mm/s, and hatch distance: 50–70  $\mu\text{m}$ . As the laser energy density is increased from 33.8 to 142.9 J/mm<sup>3</sup>, the density of the formed sample gradually increases, producing a crack-free formed sample with a density of 99.4% (Fig. 7). Then, the molten pool grain structure gradually changes, becoming a small equiaxed crystal with a grain size of only 1–2  $\mu\text{m}$  (Fig. 9). Zr-containing amorphous alloys can generate Al<sub>3</sub>Zr particles during the LPBF process of 7075 high-strength aluminum alloy, promoting the transformation of columnar crystals to equiaxed crystals and inhibiting the generation of solidification cracks (Figs. 10 and 11). The introduction of Zr-containing amorphous alloy can optimize the mechanical properties of 7075 high-strength aluminum alloy LPBF prints. The highest average microhardness value of the deposited sample reached 154.4 HV, which is 17.7% higher than that of the unmodified LPBF-printed 7075 high-strength aluminum alloy (Fig. 13).

**Conclusions** This study aims to improve the printability and quality control of the LPBF of high-strength aluminum alloys, innovatively introducing Zr-containing amorphous alloys into 7075 high-strength aluminum alloys and study the effect of Zr-containing amorphous alloy on the printing quality of 7075 high-strength aluminum alloy under different process conditions. The analysis of the single-track printing experiment shows that the laser power and scanning speed affect the size and morphology of the single melt pool. Extremely high or low laser power and scanning speeds are not conducive to the formation of stable melt tracks. Analysis of the surface roughness of single-layer printed sample shows that the size of the hatch distance affects the quality of the single-layer surface. When the overlap ratio is 60%–80%, the printing quality of a single-layer surface with a surface roughness of less than 13  $\mu\text{m}$  can be obtained. Orthogonal experimental results show that the highest density and microhardness process overlap, the optimal process parameters are laser power: 300–340 W, laser scanning speed: 600–800 mm/s, and hatch distance: 50–70  $\mu\text{m}$ . As the laser energy density increases from 33.8 to 142.9 J/mm<sup>3</sup>, the molten pool grain structure gradually transforms into fine equiaxed crystals, thereby realizing the complete grain refinement. The crack-free sample with density of 99.4% is obtained, and the hardness of the deposited sample reaches 154.4 HV. The introduction of Zr-containing amorphous alloys can achieve grain refinement in the LPBF printing process of 7075 high-strength aluminum alloy, which has a significant inhibitory effect on the solidification cracks and can improve the mechanical properties of 7075 high-strength aluminum alloy LPBF-formed samples.

**Key words** laser technique; laser powder bed fusion; high-strength aluminum alloy; solidification crack; microstructure